

HiSST: 4th International Conference on High-Speed Vehicle Science Technology 22 -26 September 2025, Tours, France



Flowfield Investigation through kHz Measurements of an Underexpanded **Jet in Hypersonic Crossflow**

Nicholas W. Stegmeier¹, Neil S. Rodrigues², Kevin R. Posladek³, Christopher S. Combs⁴

Abstract

High-speed schlieren, infrared thermography, and acetone planar laser-induced fluorescence (PLIF) were applied to an underexpanded sonic jet transversely injected into a Mach 7.2 air crossflow (Re₁ ≈ 3×10⁷ m⁻¹) in the University of Texas at San Antonio (UTSA) Ludwieg tube. Wide-field schlieren at 40 kHz captured jet startup, while 300-kHz near-field schlieren resolved bow shock breathing, shear layer flapping, and barrel shock deformation. Mid-wave infrared (IR) imaging at 4 kHz, acquired simultaneously with the 40-kHz schlieren, revealed spanwise-varying surface heating peaks and valleys driven by upstream vortices. Center-plane acetone PLIF at 10 kHz, acquired during a separate test run, visualized barrel shock topology and shear layer roll-up, providing depth-resolved context to the pathintegrated schlieren. Snapshot proper orthogonal decomposition of the schlieren and PLIF images isolated a dominant coupled bow/barrel shock mode with Strouhal number $St_{\delta} \approx 0.017$.

Keywords: hypersonic flows, jet-in-crossflow, non-intrusive diagnostics, high-speed measurements

Nomenclature

Latin

D – Jet diameter

G – One-sided power spectral density

J – Jet to crossflow momentum flux ratio

JPR – Jet exit pressure to freestream static

pressure ratio

M - Mach number

Re – Reynolds number

St – Strouhal number

f – Frequency

p – Pressure

t - Time

x – Streamwise coordinate

y – Transverse or plate-normal coordinate

z – Spanwise coordinate

Greek

δ – Boundary layer height

σ – Standard deviation

Subscripts

0 – Stagnation or total condition

1 – Unit or per length

 ∞ - Freestream condition

j – Jet

1. Introduction

Reaction control system (RCS) thrusters are used on reentry capsules and hypersonic vehicles to produce forces for attitude control. The jet-in-crossflow (JICF) flowfield generated by RCS thrusters is characterized by a highly three-dimensional shock-wave/boundary-layer interaction (SWBLI) that can elevate surface heating and complicate control law development [1-3]. Accurate prediction of both the transient loads and the local thermal environment therefore hinges on detailed knowledge of the unsteady flow physics surrounding a supersonic jet issuing into a hypersonic freestream.

HiSST-2025-21 Copyright © 2025 by author(s) Flowfield Investigation of an Underexpanded Jet in Hypersonic Crossflow

¹PhD Student, University of Texas at San Antonio, San Antonio, TX, nicholas, steameier@utsa, edu

²Optical Physicist, NASA Langley Research Center, Hampton, VA, neil.s.rodriques@nasa.gov

³PhD Student, University of Texas at San Antonio, San Antonio, TX, kevin.posladek@utsa.edu

⁴Associate Professor, University of Texas at San Antonio, San Antonio, TX, christopher.combs@utsa.edu

The canonical hypersonic JICF is comprised of a bow shock wrapped around the jet plume, an underexpanded barrel shock terminated by a Mach disk, a separated upstream boundary layer that feeds a horseshoe vortex, and a Kelvin–Helmholtz-driven shear layer that rolls up into a counter-rotating vortex pair downstream [4]. These features are illustrated in Fig. 1. Time-resolved schlieren and shadowgraph studies have shown that the bow shock, barrel shock, and separation shock all oscillate in concert with shear layer vortices [5, 6], likely influencing surface pressure and heating fluctuations [7]. Various researchers have reported broadband unsteadiness of JICF shock structures [7–9], yet most existing datasets are limited to single-frame snapshots or low kHz-rate sequences, leaving the highest frequency dynamics—and their coupling to surface loads—poorly resolved at hypersonic conditions.

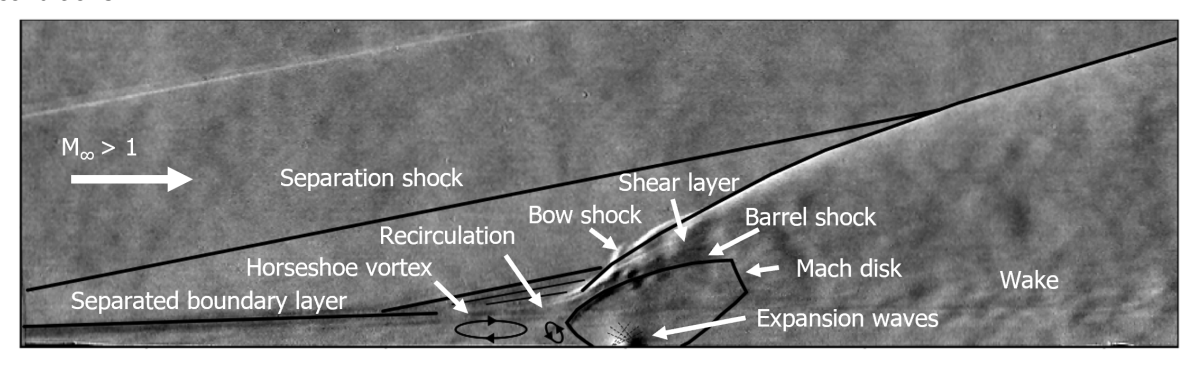


Fig 1. Supersonic JICF flow features annotated for a schlieren image of an underexpanded sonic jet in Mach 7.2 crossflow.

Optical diagnostics have progressively filled parts of this knowledge gap. Continuous high-speed schlieren has captured shock motions up to 100 kHz, but almost exclusively below Mach 6 and without simultaneous surface measurements [6, 9–11]. Infrared (IR) imaging has been employed to map qualitative heating footprints of sonic jets in supersonic crossflows, offering valuable surface information but at frame rates less than 200 Hz and without simultaneous off-surface visualization [12–15]. Planar laser-induced fluorescence (PLIF) studies—often at 10 Hz but more recently at repetition rates of 10–20 kHz—have primarily examined crossflow Mach numbers less than 7 and generally captured only isolated plume snapshots, providing limited insight into the coupled shear layer and shock dynamics [16–18]. One exception is the application of 10 kHz nitric oxide PLIF to a sonic jet in a Mach 9 crossflow by Jiang et al. [19], although this study did not present a detailed analysis of the flowfield dynamics.

In the present study we employ a suite of non-intrusive, high-speed diagnostics to interrogate a sonic underexpanded jet transversely injected into a Mach 7.2 crossflow. Qualitative IR imaging at 4 kHz records the evolving surface heating pattern generated by the jet-induced flowfield, while conventional schlieren at up to 300 kHz resolves the bow shock undulation, shear layer flapping, and barrel shock deformation. Complementary acetone PLIF at 10 kHz visualizes the near-field barrel shock and shear layer, enabling cross-diagnostic comparison. Proper orthogonal decomposition (POD) is applied to both the path-integrated schlieren data and the PLIF images, extracting the dominant spatial modes and their spectral characteristics. Collectively, these measurements aid understanding of the overall hypersonic JICF flowfield and provide validation data for numerical models.

2. Experimental Methodology

2.1. Wind Tunnel Facility

Experiments were conducted in the Mach 7.2 Ludwieg tube wind tunnel facility at the University of Texas at San Antonio. A schematic of the facility is presented in Fig. 2. Air is initially pressurized and heated within an 18-meter driver tube, achieving stagnation pressures and temperatures up to 14 MPa and 700 K, respectively. For this study, the driver tube was unheated, and the stagnation pressure was approximately 2.2 MPa. A scored diaphragm ruptures at a predetermined pressure, initiating airflow through the planar converging-diverging nozzle into the 203 mm \times 203 mm (8 in \times 8 in) test section. Diaphragm burst is detected using a 0–2000 psia pressure transducer, which can be used to trigger high-speed data acquisition systems. Downstream, flow enters a diffuser before exhausting into a 6 m³ (1600-gallon) vacuum tank. The test section is equipped with optical access designed to facilitate various diagnostic techniques, including high-speed schlieren imaging [20], PLIF [21], particle image

velocimetry (PIV) [22], molecular tagging velocimetry (MTV) [23, 24], and pressure- and temperaturesensitive paints (PSP/TSP) [25, 26]. Typical facility run times reach up to 500 ms, providing multiple steady-state intervals between reflected expansion waves, each lasting approximately 50 to 100 ms. Unit Reynolds numbers achievable in this facility span from 0.5×10^6 m⁻¹ to 200×10^6 m⁻¹. Further details on facility design, construction, and flow characterization can be found in references [27–29].

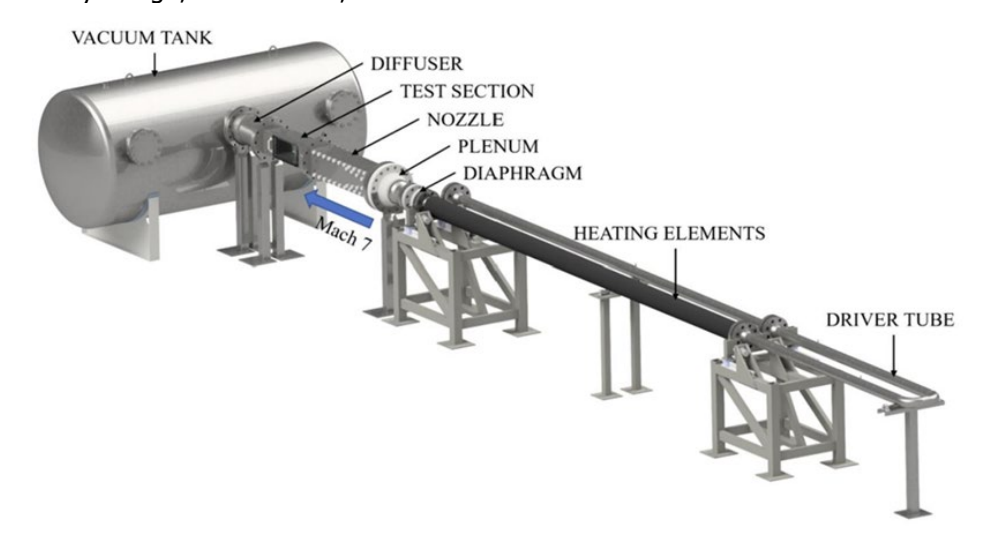


Fig 2. Rendering of the UTSA Mach 7 Ludwieg tube wind tunnel.

2.2. Experimental Apparatus

A wall-to-wall flat plate geometry was used as the basis of the experiments described here and is shown in Fig. 3. The flat plate was fabricated from stainless steel with dimensions of 445 mm \times 203 mm and a 12° leading edge. Along the centerline of the plate, a slot was machined to allow installation of interchangeable nozzle inserts. In these experiments, an insert was used that positions the nozzle outlet 143 mm from the leading edge. A hollow strut was used to position the flat plate surface at the midplane of the wind tunnel test section and to provide a convenient region for routing the jet fluid supply. The Mach 1 nozzle used in these experiments was machined from aluminum with a 1.7 mm exit diameter and a plenum-to-throat area ratio of 42.8. In this study, a Cartesian coordinate system is used with its origin at the center of the nozzle outlet with the orientation shown in Fig. 3a.

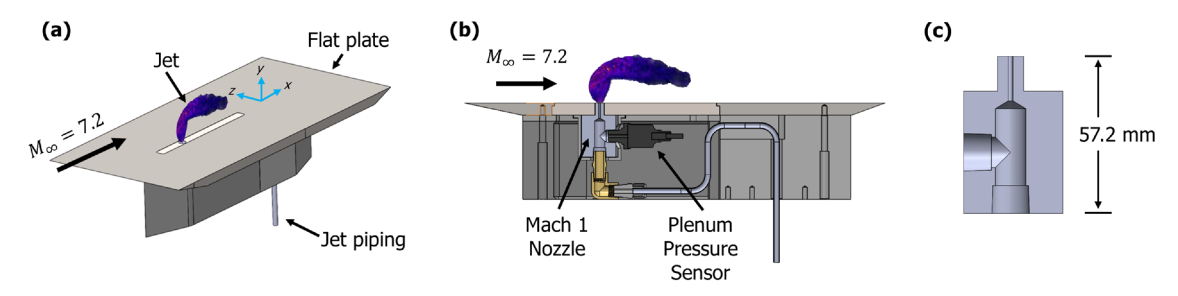


Fig 3. Flat plate with Mach 1 nozzle insert: (a) isometric view, (b) cross-section view, (c) nozzle cross-section. Jet visualization from [1].

For all experiments reported here, the jet fluid was a mixture of gaseous N_2 and acetone vapor, while the crossflow was air. The N_2 was supplied from a compressed gas bottle and the pressure was set by a regulator on the bottle. To form the mixture, the N_2 was fed through an unheated acetone bubbler, consisting of a vessel with liquid acetone and fluid lines to force the N_2 to "bubble" upwards through the liquid acetone and toward the jet nozzle. This is an effective seeding method due to the high vapor pressure of acetone at room temperature [30]. Assuming a saturated vapor mixture exiting the bubbler, the mole fraction of acetone in the jet was less than 10% for the conditions in this study, and the effect on the specific heat ratio and the resulting gas dynamics was minimal [23]. The jet stagnation pressure was monitored with an Omega® 0-3000 psia pressure sensor installed inside the hollow strut and immediately before the jet nozzle. The jet was actuated for 500 ms starting immediately after tunnel diaphragm burst using a 12V solenoid valve with a Viton seal. The opening

time of the valve was less than 30 ms, which is comparable to the time required for steady-state conditions to establish in the wind tunnel test section [29]. While Viton is not generally compatible with acetone, the short operating times for this application limited the valve seal degradation. An example pressure trace comparing the wind tunnel stagnation pressure to the jet plenum pressure is shown in Fig. 4a. In addition, the jet exit static pressure to freestream static pressure ratio (JPR) and jet-to-crossflow momentum flux ratio (J) are also shown in Fig. 4b. Note that the first steady-state period for the wind tunnel occurs from approximately 20 ms to 100 ms, while the jet plenum pressure does not plateau until around 70 ms. All statistical quantities and images were calculated for the acquisition period 70 ms to 95 ms, where the jet plenum conditions were relatively constant.

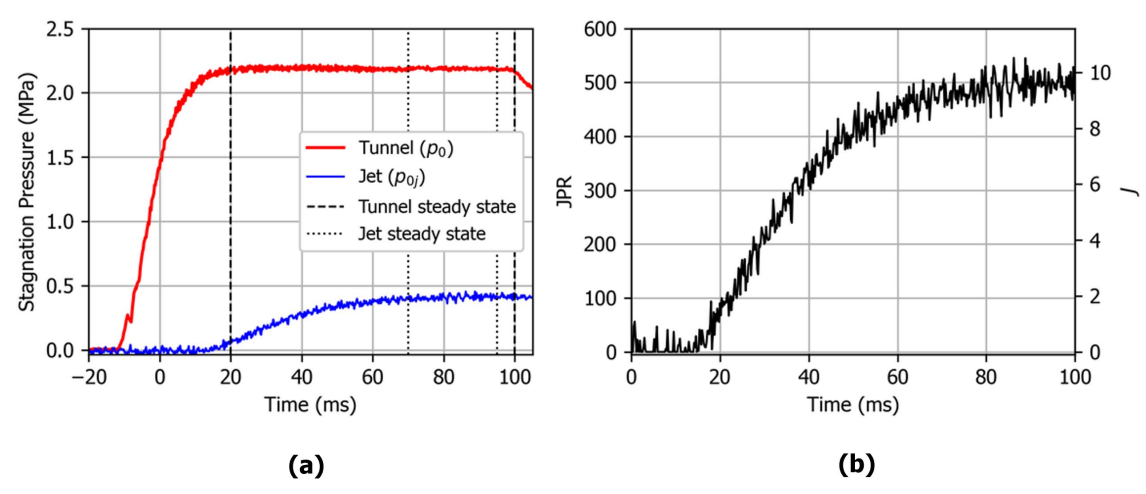


Fig 4. (a) Wind tunnel and jet stagnation pressure traces; (b) JPR (left axis) and J (right axis).

2.3. Schlieren

Schlieren imaging is a non-intrusive flow visualization technique that exploits the refractive effects of density gradients to reveal flow structures such as shockwaves and boundary layers. A conventional Z-type schlieren imaging setup [31] was used to visualize JICF flow structures through two 101.6 mm \times 101.6 mm UV-grade fused silica windows. A Luminus Devices® CBT-140 red LED and an adjustable iris were used to create a high-intensity point source. The light was collimated using two 1.52 m focal length spherical mirrors and folded into a "Z" using two flat mirrors. A razor blade was used to filter the light at the focal point. Images were acquired at 40 and 300 kHz using a Photron® FASTCAM SA-Z equipped with a Nikon® 70-200 mm f/2.8E camera lens. For the 40-kHz case, the Photron® exposure time was set to 804 ns, while for the 300-kHz case the exposure was set to 347 ns. The camera resolution was 0.114 mm/pixel. A top view of the schlieren setup is shown in Fig. 5.

The resulting schlieren images were processed using an in-house Python code for image realignment and background division. Image realignment is necessary to account for tunnel recoil after diaphragm burst. A phase-based cross-correlation method [32] was used to achieve subpixel realignment by referencing a background image taken before diaphragm burst. After realignment to the background image, lens and window artifacts were removed from the schlieren images using a background division method. Finally, the images were contrast-adjusted to enhance flow features and shockwaves.

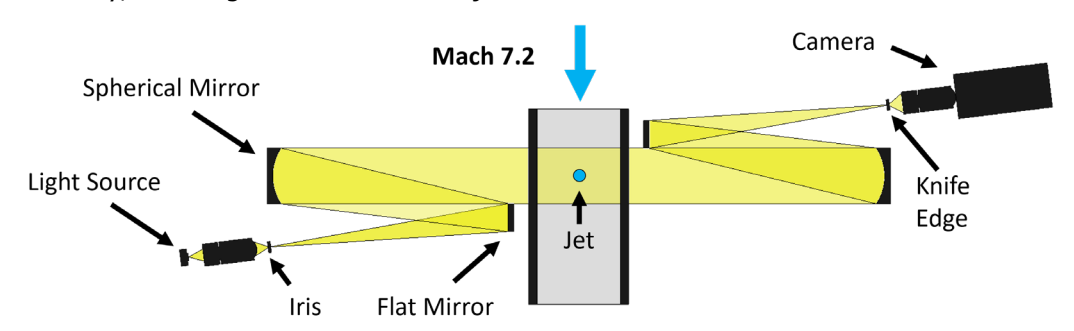


Fig 5. Schlieren setup top view.

2.4. IR Imaging

Infrared thermography offers a non-intrusive means of capturing global surface temperature distributions in wind tunnel experiments with high spatial resolution and sensitivity. The method is based on radiative heat transfer, leveraging Planck's law to relate emitted radiance to surface temperature. Accurate temperature readings depend not only on the target model but also on environmental conditions and the transmissivity of the medium within the IR band. Ideal surfaces for IR thermography behave like black bodies and have low thermal conductivity [33]. The foundational theory is detailed by Astarita and Carlomagno [34, 35].

In this study, a Telops® FAST M3K mid-wave infrared (MWIR) camera with a 50 mm lens was used to capture qualitative thermal trends at 4 kHz. The spatial resolution was 0.35 mm/pixel. Optical access was provided by an MWIR-compatible sapphire window installed in the top wall of the wind tunnel test section. To reduce reflections, imaging was conducted at an incidence angle of roughly 10°. A thin coat of black paint was applied to the flat plate and nozzle insert to enhance surface emissivity, a practice validated in prior work [36, 37]. A full radiometric calibration has not yet been performed as the data presented here are preliminary, qualitative, and intended to guide future campaigns. Raw IR frames were registered to account for tunnel recoil and background subtracted using a wind-off mean image to partially mitigate stationary reflections from the sapphire window.

2.5. Acetone PLIF

Acetone molecules seeded in the jet were excited using the 266 nm laser output from a Spectral Energies, LLC QuasiModo Nd:YAG pulse-burst laser. Data were acquired at a laser repetition rate of 10 kHz and a burst width of 10 ms, resulting in 100 laser pulses per tunnel run. Each laser pulse had a width of about 10 ns, and the beam diameter was 7 mm. The 266 nm burst energy was measured using an MKS® F100A-PF-DIF-33 thermopile sensor at the laser output port and the average per-pulse energy was calculated to be approximately 80 mJ/pulse. Under similar laser fluence and flow conditions, Andrade et al. found that acetone LIF remained in the linear (unsaturated) regime [24]. Three mirrors coated to reflect 266 nm laser light were used to direct the laser beam toward the wind tunnel test section. Before entering the test section, the beam was formed into a streamwise-parallel sheet using a +500 mm spherical lens and a -100 mm cylindrical lens. The sheet expanded to a width of approximately 20 mm at the nozzle exit. The focusing lens was positioned so that the beam waist occurred 10 mm above the nozzle exit, and the sheet was ~1 mm thick at the waist. The sheet intercepted the flat plate along the jet nozzle centerline, extending several jet diameters upstream and downstream of the nozzle exit. Optical access for the laser sheet was afforded by a 25.4 mm × 76.2 mm UV-grade fused silica window installed on the top wall of the test section. The sheet forming optics are shown schematically in Fig. 6a and a picture of the wind tunnel setup is shown in Fig. 6b.

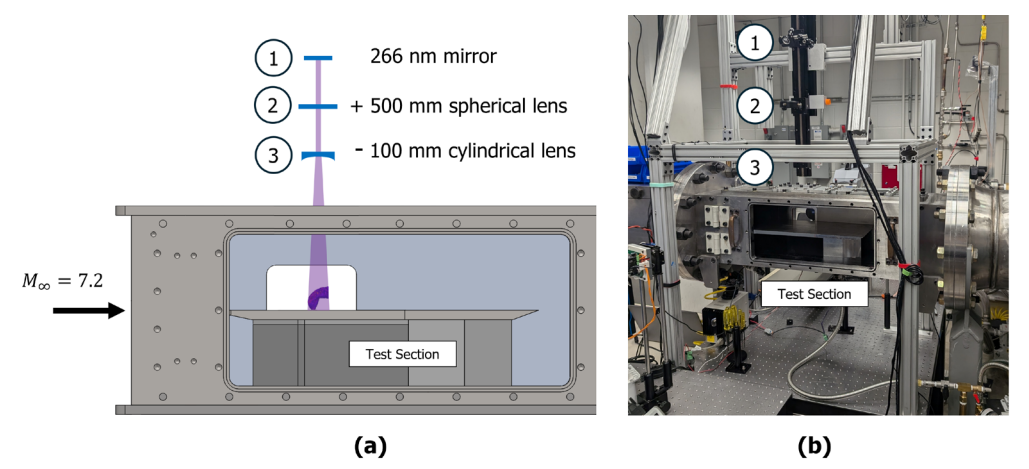


Fig 6. PLIF sheet-forming optics: (a) digital rendering, (b) laboratory setup (flow left-to-right).

PLIF images were acquired using a Photron[®] FASTCAM SA-Z equipped with a LaVision[®] High Speed IRO-X S20 intensifier and a Sigma[®] 105mm f/2.8 Macro lens. The resolution was 0.051 mm/pixel. The intensifier gain was set to 98%. The optical elements internal to the camera lens effectively filtered the 266 nm UV laser light, so a UV filter was not deemed necessary. The laser synchronization signal from the burst-mode laser oscillator was used to synchronize the laser, camera, and intensifier. The timing

of the laser pulses was determined using a ThorLabs[®] DET10A2 photodiode. Using an oscilloscope to monitor the waveforms and the laser pulses, delays were introduced to the camera and intensifier so that the laser pulse occurred approximately in the middle of both the camera exposure and the intensifier gate. The camera exposure was set to 98.4 µs while the intensifier gate was 500 ns. The acetone fluorescence lifetime is expected to be less than 250 ns for this application [38]. At freestream velocities, this gating would permit significant motion blur. However, structures in the JICF shear layer convect more slowly. For a shear layer convective speed of 340 m/s, the upper-bound blur using the 500 ns gate is 3.3 px, while a lifetime-limited 250 ns effective exposure yields 1.7 px. The laser pulse train and image acquisition were delayed 70 ms after diaphragm burst using an SRS[®] digital delay generator to ensure steady-state conditions for both the wind tunnel and jet.

2.6. Proper Orthogonal Decomposition

Proper Orthogonal Decomposition (POD) is a modal decomposition technique that represents an unsteady field as a weighted sum of spatial modes ordered by the variance they capture [39]. For an image sequence, each frame is reshaped into a column vector; stacking all columns yields a data matrix whose singular value decomposition consists of orthonormal spatial modes, their corresponding singular values, and temporal coefficients describing the time evolution of each mode. The approach isolates dominant flow structures [40, 41] and provides compact, noise-robust reconstructions that are well suited for statistical or spectral analysis of large image datasets [42]. In this study, the open source Python package <code>modred</code> [43] was used to apply snapshot POD to the steady-state 300-kHz schlieren and 10-kHz acetone PLIF. For the schlieren dataset, Welch's method [44] was used to estimate the power spectral density (PSD) curves of the POD mode temporal coefficients with a block size of 1024 and 50% overlap, yielding 13 blocks in total and a frequency resolution of 293 Hz. Of the 100 PLIF images, 92 consecutive frames were selected with sufficient signal-to-noise ratio (SNR) for modal analysis. With so few samples, higher order modes may not be fully converged [45], and Welch averaging is not possible. However, the leading modes were found to be robust in that splitting the dataset yielded the same dominant mode structures.

2.7. Experimental Matrix

Three wind tunnel experiments were selected from a broader campaign for detailed analysis and discussion in this study. Because the parent campaign was exploratory in nature, aimed at developing the best practices for JICF diagnostics in the UTSA wind tunnel, the experiments span a variety of diagnostic techniques (schlieren, IR, and PLIF), acquisition rates (4-300 kHz), jet parameters, and fields of view. In general, the cases have been categorized as "Low JPR" or "High JPR" and are shown in Table 1. The low-JPR case combines wide-field schlieren (40 kHz) with plan-view IR thermography (4 kHz), capturing global jet startup features and the approach to steady state. The high-JPR cases comprised two datasets: (i) near-field 300-kHz schlieren, resolving bow shock and shear layer dynamics, and (ii) 10-kHz acetone PLIF, which isolated center-plane shear layer features. For all tests, the unit Reynolds number (Re₁) was approximately (3.0±0.24)×10⁷ m⁻¹, likely resulting in a laminar or transitional boundary layer (δ =2.5 mm) upstream of the JICF interaction, as indicated by traversing pitot probe scans on a flat plate in similar conditions in the UTSA wind tunnel [22]. The jet plenum pressure sensor was inoperative for the high-JPR cases, so the pressure regulator reading was used to calculate the jet parameters. There is a pressure drop between the regulator and the nozzle plenum due to passage through the bubbler and piping, but it was not quantified for this study. The wind tunnel and jet stagnation temperatures were assumed to be room temperature for all cases. Freestream and nozzle exit conditions were calculated using isentropic relations. For the low-JPR case, the instantaneous measurement uncertainties were ±3.0 for J and ±176 for JPR, with the largest uncertainty source being jet plenum pressure measurement.

Re₁ (m⁻¹) **Diagnostics** Rate (kHz) p₀ (MPa) p_{0j} (MPa) J JPR 3.0×10^{7} Schlieren/IR 40/4 2.20 0.40 9.2 475 300 2.9×10^{7} 859 Schlieren 2.10 0.69 16.6

2.20

0.69

Table 1: Flow Conditions and Diagnostics

 3.0×10^{7}

10

Case

Low JPR

High JPR

High JPR

PLIF

15.9

822

3. Results

3.1. Steady-State Flowfield

The mean steady-state flowfield for the low-JPR case is illustrated in Fig. 7. Many of the canonical JICF flow features such as the separation shock, bow shock, and barrel shock can be identified in Fig. 7a, as previously annotated in Fig. 1. The surface thermal trends clearly show the three-dimensional nature of the flow and indicate complex interactions occurring upstream and downstream of the jet. The boundary layer separation shock foot occurs upstream and out of the field of view. While the separation shock is visible in the mean schlieren, potential surface effects (in the region -25 < x/D < -10) are obscured by a combination of low SNR and background artifacts. In the region -10 < x/D < 0, and wrapping around the jet, a pattern of temperature peaks and valleys exists. In blunt-body SWBLI flowfields, upstream heating maxima occur where counter-rotating vortices produce stagnation points on the surface, and minima where vortices pull fluid away from the wall [46]. These minima and maxima can also be associated with flow separation and attachment, respectively [47]. In JICF, the number of vortices upstream of the jet has been shown to vary with JPR, with higher pressure ratios typically producing more upstream vortices [48] and much larger recirculation zones [49]. Notably, not all the upstream vortices persist downstream as horseshoe vortices [48, 50], and some authors have indicated that the canonical horseshoe vortex originates from recirculating fluid upstream of the bow shock [47], and others downstream [50]. Given these complexities, identifying the exact flow structures responsible for the complex heating pattern seen here will likely require further experiments, such as oil flow or particle tracking methods in the separated region. Some tentative identifications of the thermal patterns are provided in Fig. 7b.

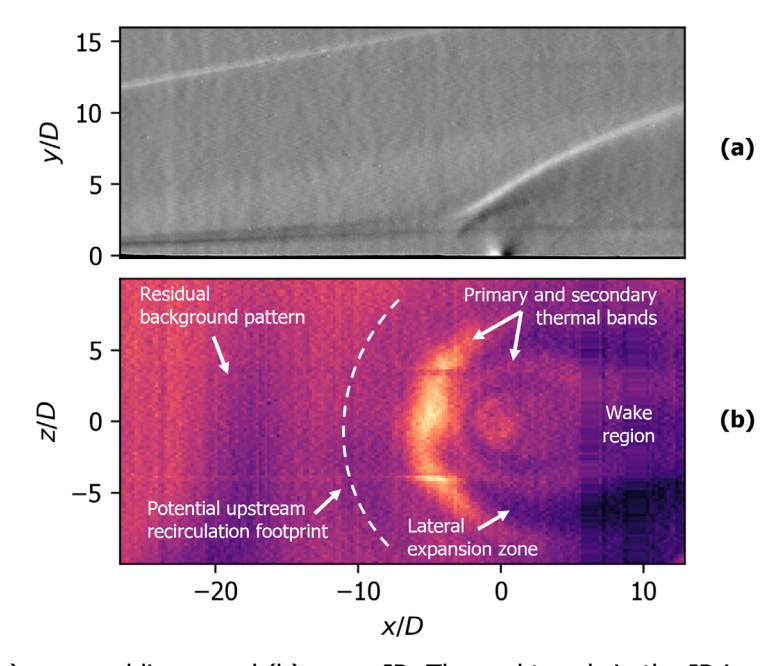


Fig 7. Low-JPR (a) mean schlieren and (b) mean IR. Thermal trends in the IR imagery correlate with shock structures in the schlieren.

3.2. Jet Startup

With one of the primary applications of JICF being control authority, it is critically important to understand the dynamics of jet startup, as these dynamics result in the transient forces on an aerospace vehicle. Fig. 8 shows schlieren and IR images for the low-JPR jet startup sequence. Because the tunnel reaches steady state 20 ms after burst, this sequence of images shows how varying the jet plenum pressure and jet parameters (J, JPR) affect the spatial extent of the shock structures and surface heating profile. The relevant pressure traces are shown in Fig. 4. Previous work has shown that the spatial extent of the underexpanded plume increases linearly with momentum flux ratios between 5 and 35 [17], and this is qualitatively confirmed by cross-comparison of the momentum flux trace in Fig. 4b and the shock structures in Fig. 8. The IR-imaged thermal trends also appear to follow this trend because the upstream recirculation zone is pushed further upstream as the underexpanded jet grows in extent.

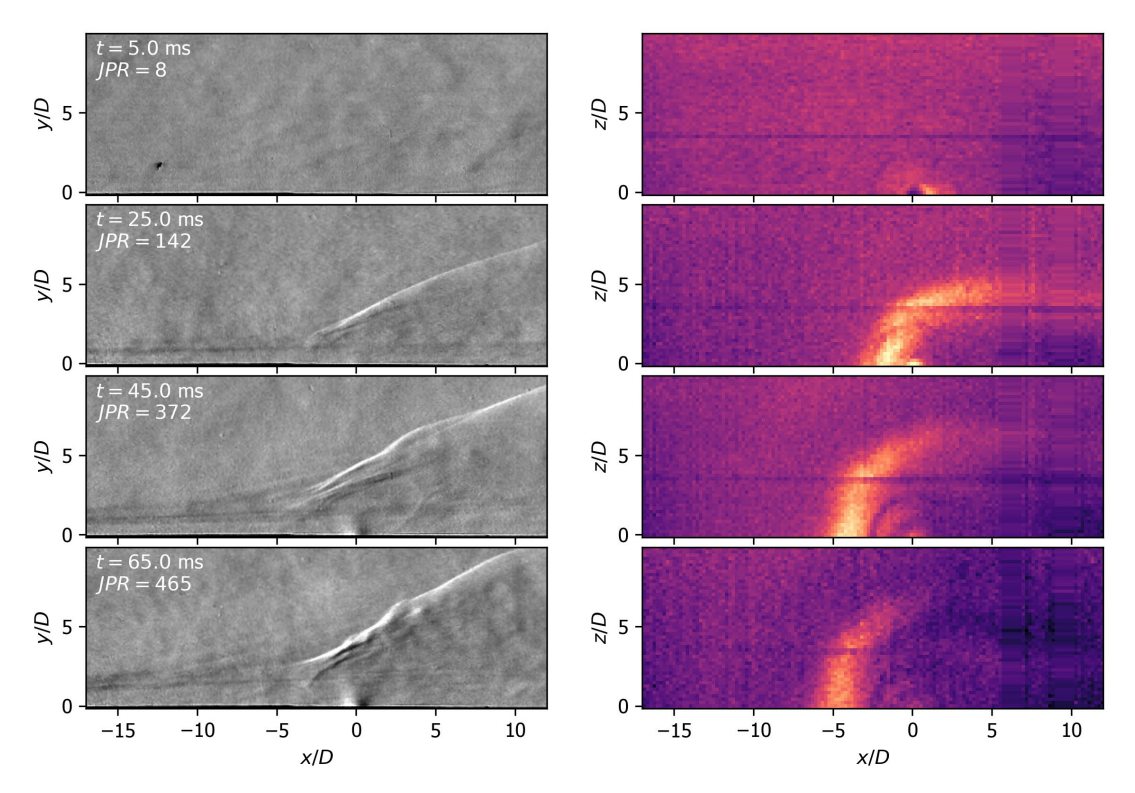


Fig 8. Sequence illustrating jet startup with (left) schlieren and (right) plan-view IR for the low-JPR case. Only the top half (z/D > 0) of the streamwise symmetry plane is shown for the IR images.

3.3. Time-resolved Schlieren

The steady-state dynamics of the jet near-field were investigated with 300-kHz schlieren for the high-JPR case. The mean and standard deviation schlieren images are shown in Fig. 9. At higher frame rates, less of the camera sensor is available for imaging due to memory bandwidth constraints, and the smaller field of view is immediately evident in Fig. 9a. Nonetheless, the near-field JICF flow structures are evident, including the boundary layer, bow shock, barrel shock, and underexpanded jet expansion waves. Note that the boundary layer appears darker because a diagonal knife edge was used for the schlieren setup of the high-JPR case, whereas a vertical knife edge was used for the low-JPR case. Time-resolved videos of this flowfield reveal a highly dynamic bow shock and shear layer, as evidenced by the bright band in Fig. 9b.

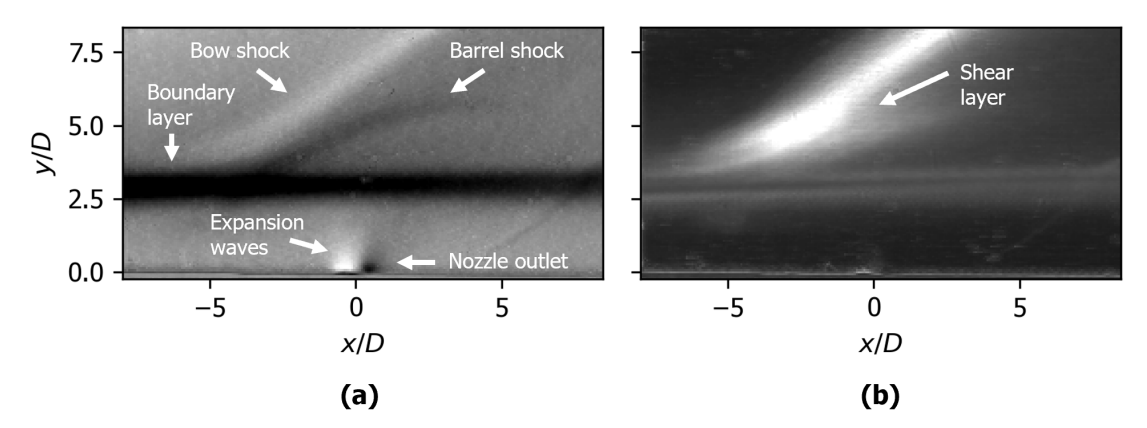
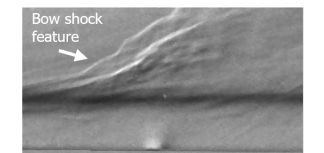
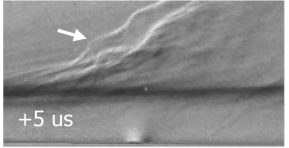


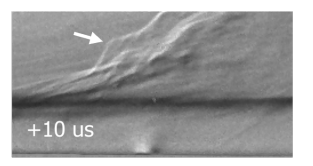
Fig 9. High-JPR case (a) mean and (b) standard deviation schlieren images.

The 300-kHz acquisition rate allows frame-by-frame tracking of undulations in the JICF bow shock. In Fig. 10, a bow shock "bubble" is tracked as it emerges from the upstream portion of the bow shock and travels downstream. The bubble appears to grow as it is convected downstream over a time period of approximately 15 μ s. Based on the physical dimensions, this corresponds to an average streamwise convection speed of approximately 340 m/s, significantly slower than the freestream velocity of 886

m/s [23]. This observation is consistent with measurements by Ben-Yakar, who found that shear layer structures did not reach freestream velocities until many diameters downstream of the jet orifice [5].







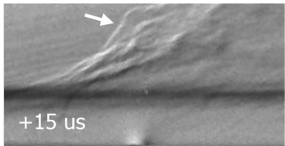


Fig 10. Time-resolved sequence of schlieren images with a "bubble" traveling downstream along the bow shock.

To shed light on the bow shock and shear layer dynamics, POD was performed on the schlieren images. The resulting mode energies are shown in Fig. 11 and the first 20 POD modes are shown in Fig. 12. The first 20 POD modes contain over 40% of the total energy, whereas 120 modes are required to capture over 80% of the energy. The large number of modes required to capture the variance in the images indicates a broad range of spatial scales and spectral content. The first and most energetic mode displays large-scale breathing of the bow shock and barrel shock with a pattern resembling dominant POD modes for schlieren of cylinder SWBLI [40]. Some modes (3, 6, 14, & 15 in Fig. 12) capture lifting and lowering of the boundary layer, perhaps related to coupling between the separated flow ahead of the jet and shock structures in the JICF near-field. Finer spatial patterns in the bow shock are captured with increasing mode number. Physical interpretation of the modes, however, is constrained by the path-integrated nature of conventional schlieren. Because each pixel integrates the streamwise density gradient field, POD modes may optimally capture image variance by superposing contributions from multiple spanwise locations. A single mode may therefore mingle physically unrelated structures, as potentially illustrated by mode 15, whose rippled bow shock pattern may arise from different spanwise coherent structures acting out of phase. Complementary diagnostics such as PLIF are required to disentangle such superposed effects and assign modes unambiguously to specific threedimensional features. Despite these projection limits, features whose density gradients are isolated or add coherently along the viewing direction—such as the centerline crest of the bow shock and the rounded rim of the barrel shock—remain comparatively easy to interpret.

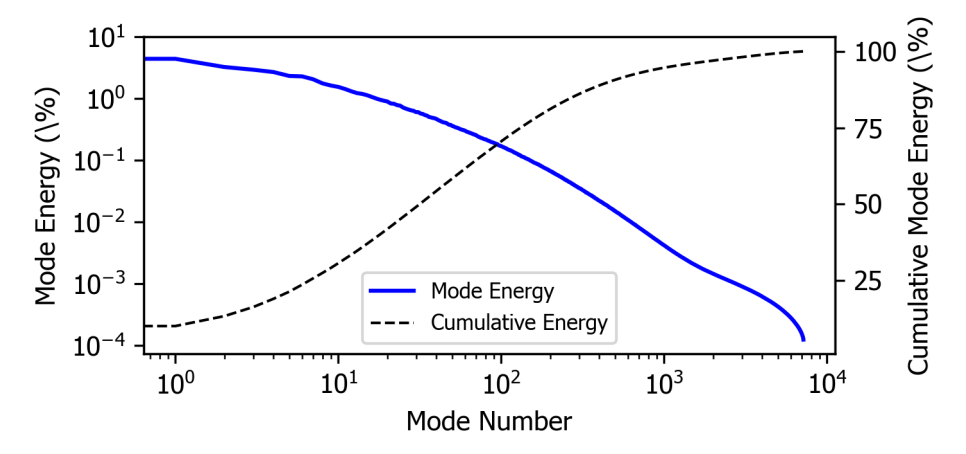


Fig 11. POD mode energies (left axis) and cumulative energy (right axis).

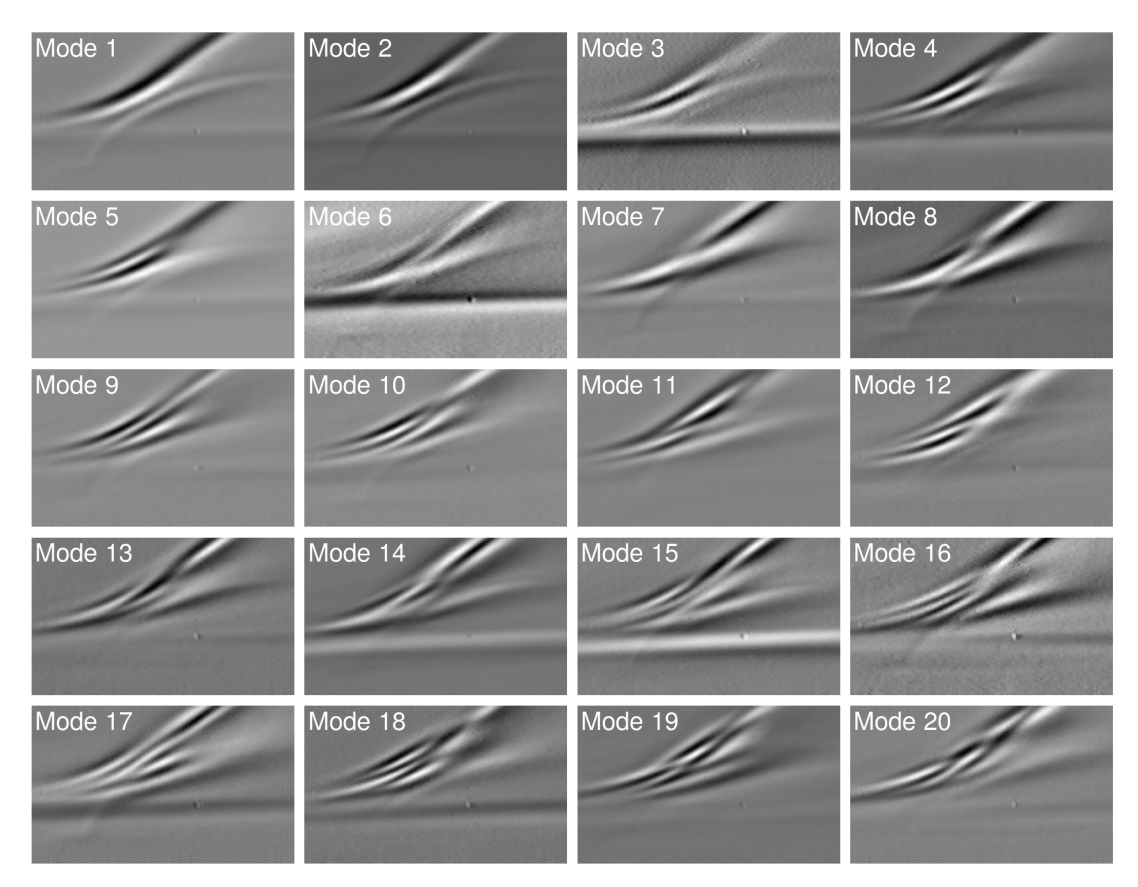


Fig 12. POD modes 1-20. The dominant modes capture bow shock, barrel shock, and boundary layer fluctuations (e.g., modes 1-3). Higher order modes capture finer spatial patterns such as ripples in the bow shock.

Although standard POD does not impose a frequency or phase constraint on the modes, the temporal coefficients associated with each mode carry spectral content. Fig. 13 shows frequency pre-multiplied Welch power spectra normalized by the pixel intensity variance for a selection of modes. The Strouhal number was calculated using the boundary layer thickness upstream of the jet and the nozzle exit diameter. Mode 1, associated with large-scale movement of the bow shock, has a spectral peak near $St_{\delta} = 0.017$ or $St_{D} = 0.011$, reminiscent of the low-frequency spectral content characteristic of SWBLI [51]. With increasing mode number, the spectral peak shifts toward higher frequencies.

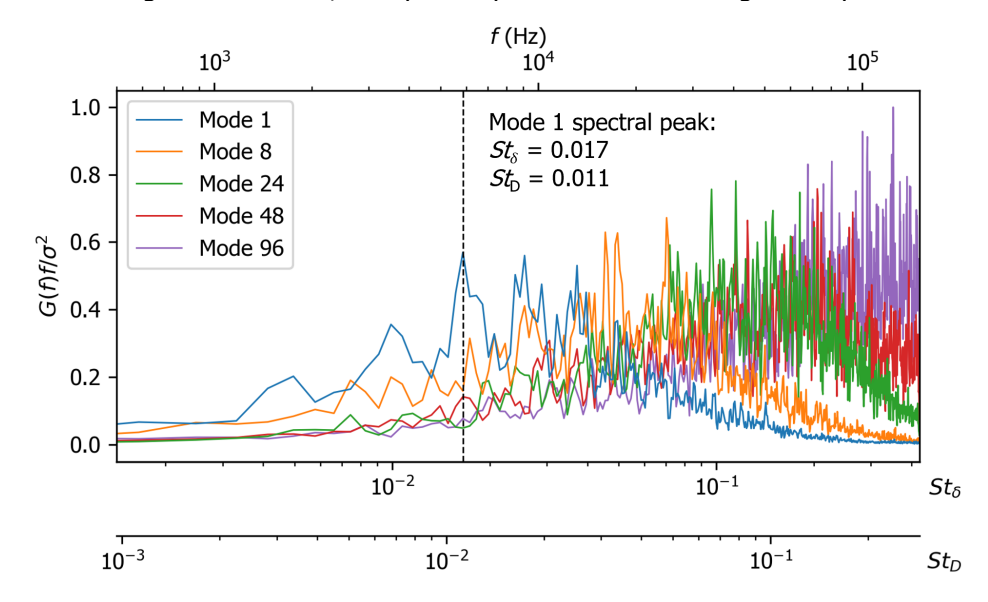


Fig 13. Normalized power spectra for select schlieren POD modes.

3.4. Acetone PLIF

To supplement the path-integrated schlieren visualization, 10-kHz acetone PLIF was employed to visualize center-plane flow structures of the JICF interaction. The acquisition rate was not sufficient to time-resolve the flow, so the instantaneous images are uncorrelated in time. Several instantaneous PLIF images are shown in Fig. 14 to illustrate the flow structures and various shear layer morphologies observed in the dataset. Due to a bright interaction between the laser sheet and surface of the flat plate, the field of view was raised approximately one jet diameter above the surface to avoid damaging the intensifier. The PLIF signal intensity is brightest near the nozzle outlet, where the number density of the fluorescing acetone molecules is relatively high. As the jet fluid expands toward the barrel shock, the signal intensity decreases. After passing through the barrel shock, the jet fluid is recompressed, and signal intensity increases. The transverse velocity of the jet is significantly decreased by the barrel shock, and the jet fluid is swept downstream as it mixes with the crossflow. Turbulent structures are evident in the shear layer with larger coherent structures developing intermittently. These large coherent structures are the cause of bow shock "bubbles" observed in Fig. 10. As shown in Fig. 15, the mean PLIF aligns closely with the flow features observed in the high-JPR schlieren.

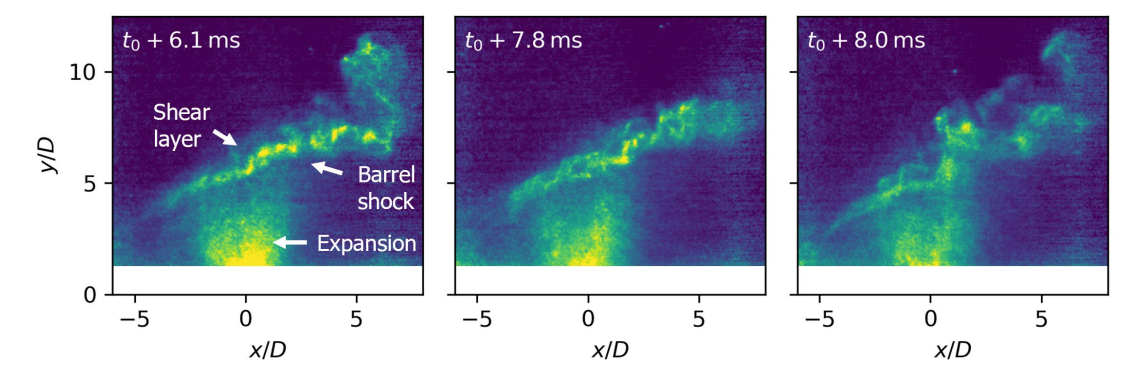


Fig 14. Instantaneous acetone PLIF images of hypersonic JICF. The laser pulse burst was initiated at $t_0 = 70$ ms after wind tunnel diaphragm burst.

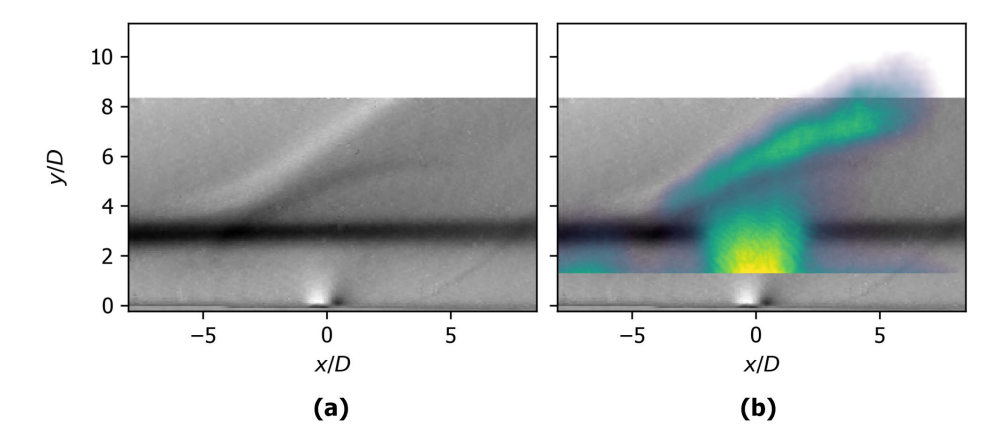


Fig 15. Comparison of schlieren and PLIF for the high-JPR cases: (a) mean schlieren and (b) mean PLIF overlaid on the mean schlieren.

To supplement the modal analysis of the high-JPR schlieren, POD was performed on the acetone PLIF image set and the leading 12 modes are shown in Fig. 16. While a sheet correction was performed on the images, mode 1 still captures gross spatial changes in sheet intensity and potential reflections from the laser sheet on the flat plate surface. Modes 2 and onwards, however, capture shear layer and bow shock fluctuations. Mode 2 bears resemblance to the leading mode of the schlieren POD, supporting the hypothesis that this mode captures large-scale bow shock, shear layer, and barrel shock fluctuations along the JICF interaction centerline. Note that none of the modes imaged in Fig. 16 show activity inside the barrel shock, whereas many of the modes in Fig. 12 show the ripples of the bow shock superimposed on the barrel shock region due to schlieren path integration.

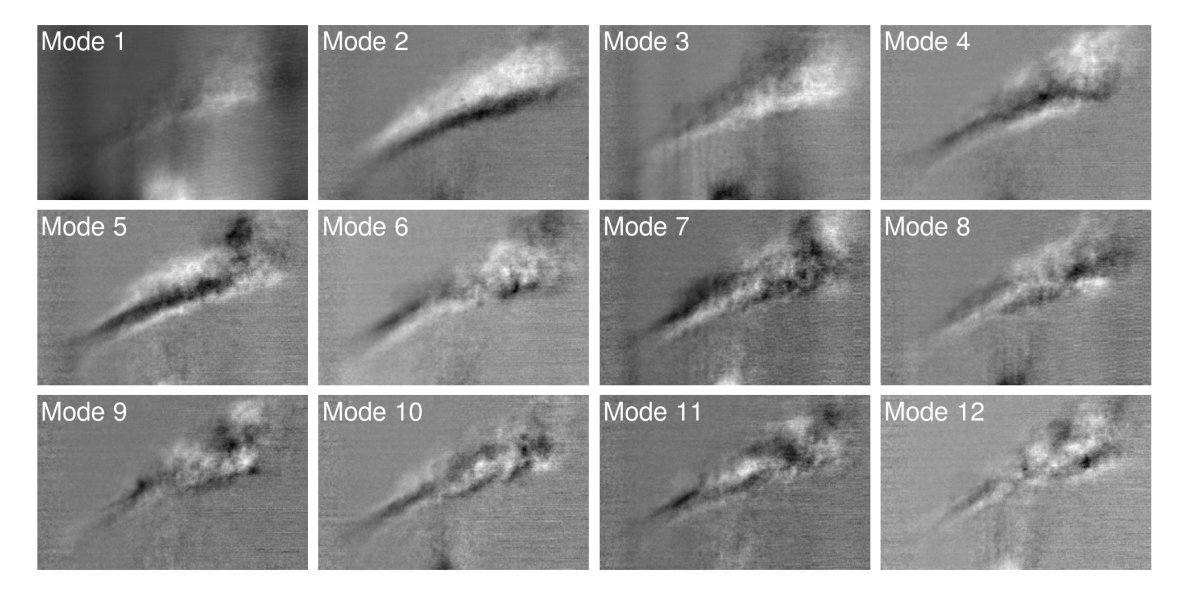


Fig 16. JICF acetone PLIF POD modes 1-12. Mode 1 captures some shear layer activity but is polluted by spatial and temporal variation in the laser sheet. Modes 2 and 3 capture large-scale shear layer activity and resemble dominant modes from the schlieren POD analysis.

4. Summary and Ongoing Work

A transverse underexpanded sonic jet issuing from a flat plate into Mach 7.2 crossflow was investigated using schlieren, IR imaging, and acetone PLIF. Global flow features and the jet startup sequence were imaged with 40-kHz schlieren of the streamwise plane and 4-kHz plan-view IR. Qualitative thermal trends indicate complex, vortex-driven surface heating. Schlieren at 300 kHz allowed investigation of the JICF near-field dynamics, including time-resolved imaging of bow shock undulations. Modal analysis indicated large-scale bow shock and barrel shock oscillation with a spectral peak near $St_{\delta}=0.017$. To complement the path-integrated schlieren images, acetone PLIF was used to image the jet barrel shock and shear layer along the center-plane. Coherent structures observed in the acetone PLIF shear layer supported conclusions made from the schlieren imagery. Modal analysis was applied to the PLIF images, and the leading modes were comparable to those seen for the schlieren. Future work will include high-speed acetone PLIF (>100 kHz repetition rate) and investigation of JICF for supersonic nozzles.

5. Acknowledgements

This work is supported by the 2024 NSTGRO Fellowship through the National Aeronautics and Space Administration under Grant No. 80NSSC24K1388.

References

- Ivey, C., Danehy, P., Bathel, B., Dyakonov, A., Inman, J., Jones, S.: Comparison of PLIF and CFD Results for the Orion CEV RCS Jets. In: 49th AIAA Aerospace Sciences Meeting including the New Horizons Forum and Aerospace Exposition. American Institute of Aeronautics and Astronautics, Orlando, Florida (2011)
- 2. Combs, C.S., Clemens, N.T., Danehy, P.M., Bathel, B., Parker, R., Wadhams, T., Holden, M., Kirk, B.: Fluorescence Imaging of Reaction Control Jets and Backshell Aeroheating of Orion Capsule. J. Spacecr. Rockets. 52, 243–252 (2015). https://doi.org/10.2514/1.A32946
- 3. Cassel, L.A.: Applying Jet Interaction Technology. J. Spacecr. Rockets. 40, 523–537 (2003). https://doi.org/10.2514/2.3992
- 4. Gruber, M.R., Nejad, A.S., Chen, T.H., Dutton, J.C.: Mixing and Penetration Studies of Sonic Jets in a Mach 2 Freestream. J. Propuls. Power. 11, 315–323 (1995). https://doi.org/10.2514/3.51427
- 5. Ben-Yakar, A.: Experimental investigation of mixing and ignition of transverse jets in supersonic crossflows, https://www.proquest.com/docview/219982301/abstract/48F5F50BB94F4154PQ/1, (2001)

- Zhang, Z., McCreton, S.F., Awasthi, M., Wills, A.O., Moreau, D.J., Doolan, C.J.: The flow features 6. of Transverse Jets In Supersonic Crossflow. Aerosp. Sci. Technol. 118, 107058 (2021). https://doi.org/10.1016/j.ast.2021.107058
- Liu, X., Zhong, J., Dong, Z., Fan, X., Zou, D., Liu, Y., Peng, D.: Low-frequency large-scale 7. unsteadiness analysis of lateral jet interactions on a slender cylinder in hypersonic flows using fast-responding pressure-sensitive paint. Exp. Therm. Fluid Sci. 152, 111113 (2024). https://doi.org/10.1016/j.expthermflusci.2023.111113
- Crafton, J., Forlines, R., Palluconi, S., Hsu, K., Carter, C., Gruber, M.: Investigation of Transverse Jet Injection in a Supersonic Crossflow Using Fast Responding Pressure-Sensitive Paint. In: 29th AIAA Applied Aerodynamics Conference. American Institute of Aeronautics and Astronautics
- Munuswamy, N., Govardhan, R.N.: Shock wave boundary layer interactions in sonic gas jet 9. injection into supersonic crossflow. Exp. Fluids. 63, 141 (2022). https://doi.org/10.1007/s00348-022-03488-5
- Stahl, B., Siebe, F., Gülhan, A.: Hot-Gas Side Jet in a Supersonic Freestream, J. Spacecr, Rockets. 47, 957–965 (2010). https://doi.org/10.2514/1.43670
- Erdem, E., Kontis, K.: Experimental investigation of sonic transverse jets in Mach 5 crossflow. Aerosp. Sci. Technol. 110, 106419 (2021). https://doi.org/10.1016/j.ast.2020.106419
- 12. Bae, J.-Y., Kim, J., Lee, N., Bae, H.M., Cho, H.H.: Measurement of surface heat transfer caused by interaction of sonic jet and supersonic crossflow near injection hole. Aerosp. Sci. Technol. 119, 107180 (2021). https://doi.org/10.1016/j.ast.2021.107180
- Gülhan, A., Schütte, G., Stahl, B.: Experimental Study on Aerothermal Heating Caused by Jet-13. Hypersonic Crossflow Interaction. J. Spacecr. Rockets. 45, 891-899 (2008). https://doi.org/10.2514/1.35899
- Singh, A., Threadgill, J.A., Berry, M.: Transverse Jet in a Mach 2 Cross-Flow on an Inclined Ogive-Cylinder. In: AIAA SCITECH 2025 Forum. American Institute of Aeronautics and Astronautics (2025)
- Kim, J., Lee, N., Bae, H.M., Bae, J.-Y., Cho, H.H.: Heat transfer measurement near injection hole of supersonic nozzle with a sonic jet injection. Aerosp. Sci. Technol. 152, 109369 (2024). https://doi.org/10.1016/j.ast.2024.109369
- Takahashi, H., Hirota, M., Oso, H., Masuya, G.: Measurement of Supersonic Injection Flowfield Using Acetone PLIF. Trans. Jpn. Soc. Aeronaut. Space Sci. 51, 252-258 (2009). https://doi.org/10.2322/tjsass.51.252
- 17. Luo, K., Chen, X., Wang, Y., Wang, Q., Yu, J., Zhao, W.: Experimental Investigation of Transverse Jet Interaction in Low-Density Hypersonic Crossflows. AIAA J. 0, 1–14 (2025). https://doi.org/10.2514/1.J065093
- 18. Miller, V.A., Troutman, V.A., Mungal, M.G., Hanson, R.K.: 20 kHz toluene planar laser-induced fluorescence imaging of a jet in nearly sonic crossflow. Appl. Phys. B. 117, 401–410 (2014). https://doi.org/10.1007/s00340-014-5849-3
- Jiang, N., Bruzzese, J., Patton, R., Sutton, J., Yentsch, R., Gaitonde, D.V., Lempert, W.R., Miller, J.D., Meyer, T.R., Parker, R., Wadham, T., Holden, M., Danehy, P.M.: NO PLIF imaging in the CUBRC 48-inch shock tunnel. Exp. Fluids. 53, 1637-1646 https://doi.org/10.1007/s00348-012-1381-6
- Hoffman, E.N.A.: Effects of surface roughness on shock-wave/boundary-layer interactions at Mach 7.2, https://www.proguest.com/dissertations-theses/effects-surface-roughness-on-shockwave-boundary/docview/2819921197/se-2, (2023)
- Stegmeier, N.W., Williamson, C., Andrade, A., Combs, C.S.: Experimental Design and Preliminary Results for Sonic and Supersonic Transverse Jets in Mach 7 Crossflow. In: AIAA AVIATION FORUM AND ASCEND 2024. American Institute of Aeronautics and Astronautics (2024)
- 22. Colborn, J.G., Stegmeier, N.W., LaLonde, E.J., Andrade, A., Combs, C.S.: Investigation of Roughness Effects on Shock-Wave Boundary-Layer Interactions Using Planar Laser Scattering. In: AIAA AVIATION FORUM AND ASCEND 2025. American Institute of Aeronautics and Astronautics
- Andrade, A., Hoffman, E.N.A., LaLonde, E.J., Combs, C.S.: Velocity measurements in a hypersonic flow using acetone molecular tagging velocimetry. Opt. Express. 30, 42199 (2022). https://doi.org/10.1364/OE.474841

- 24. Andrade, A., Shoemake, W.L., Willamson, C.O., Stegmeier, N.W., Posladek, K.R., Strasser, N.S., Hall, C.L., Olshefski, K.T., Nutter, N.F., Glasby, R.S., Combs, C.S.: Hypersonic wake velocity measurements using acetone molecular tagging velocimetry. Appl. Opt. 64, 1933–1942 (2025). https://doi.org/10.1364/AO.546880
- 25. Posladek, K., Andrade, A., Combs, C., Glasby, R.S.: Investigation of Hypersonic Double Cone Shock-Wave/Boundary-Layer Interactions Using Temperature-Sensitive Paint. In: AIAA AVIATION FORUM AND ASCEND 2024. American Institute of Aeronautics and Astronautics
- 26. Dhanagopal, A., Williamson, C., LaLonde, E.J., Gutierrez, S., Andrade, A., Delgado, V., Combs, C.S.: High-Speed Pressure Sensitive Paint Measurements of the Initial Concept 3.X Vehicle at Mach 7. In: AIAA SCITECH 2023 Forum. American Institute of Aeronautics and Astronautics, National Harbor, MD & Online (2023)
- 27. Bashor, I., Hoffman, E., Gonzalez, G., Combs, C.S.: Design and Preliminary Calibration of the UTSA Mach 7 Hypersonic Ludwieg Tube. In: AIAA Aviation 2019 Forum. American Institute of Aeronautics and Astronautics (2019)
- 28. Hoffman, E.N., Bashor, I., Combs, C.S.: Construction of a Mach 7 Ludwieg Tube at UTSA. In: AIAA AVIATION 2020 FORUM. American Institute of Aeronautics and Astronautics (2020)
- 29. Hoffman, E.N.A., LaLonde, E.J., Andrade, A., Chen, I., Bilbo, H.A., Combs, C.S.: Flow Characterization of the UTSA Hypersonic Ludwieg Tube. Aerospace. 10, 463 (2023). https://doi.org/10.3390/aerospace10050463
- 30. Thurber, M.C.: Acetone laser-induced fluorescence for temperature and multiparameter imaging in gaseous flows, https://login.libweb.lib.utsa.edu/login?url=https://www.proquest.com/dissertations-theses/acetone-laser-induced-fluorescence-temperature/docview/304536421/se-2, (1999)
- 31. Settles, G.S.: Schlieren and shadowgraph techniques: visualizing phenomena in transparent media. Springer, Berlin Heidelberg (2001)
- 32. Guizar-Sicairos, M., Thurman, S.T., Fienup, J.R.: Efficient subpixel image registration algorithms. Opt. Lett. 33, 156–158 (2008). https://doi.org/10.1364/OL.33.000156
- 33. Running, C.L., Rataczak, J.A., Zaccara, M., Cardone, G., Juliano, T.J.: A wrap-film technique for infrared thermography heat-transfer measurements in high-speed wind tunnels. Exp. Therm. Fluid Sci. 135, 110604 (2022). https://doi.org/10.1016/j.expthermflusci.2022.110604
- 34. Astarita, T., Carlomagno, G.M.: Infrared Thermography for Thermo-Fluid-Dynamics. Springer, Berlin, Heidelberg (2013)
- 35. Carlomagno, G.M., Cardone, G.: Infrared thermography for convective heat transfer measurements. Exp. Fluids. 49, 1187–1218 (2010). https://doi.org/10.1007/s00348-010-0912-2
- 36. Bur, R., Chanetz, B.: Experimental study on the PRE-X vehicle focusing on the transitional shockwave/boundary-layer interactions. Aerosp. Sci. Technol. 13, 393–401 (2009). https://doi.org/10.1016/j.ast.2009.092
- 37. Dieudonne, W., Boerrigter, H., Charbonnier, J.: Hypersonic flow on a blunted cone—flare and in the VKI-H3 mach 6 wind tunnel. Von Karman Institute for Fluid Dynamics, Rhode-Saint-Genèse, Belgium (1997)
- 38. Breuer, G.M., Lee, E.K.C.: Fluorescence decay times of cyclic ketones, acetone, and butanal in the gas phase. J. Phys. Chem. 75, 989–990 (1971). https://doi.org/10.1021/j100677a029
- 39. Berkooz, G., Holmes, P., Lumley, J.L.: The Proper Orthogonal Decomposition in the Analysis of Turbulent Flows. Annu. Rev. Fluid Mech. 25, 539–575 (1993). https://doi.org/10.1146/annurev.fl.25.010193.002543
- Hoffman, E.N.A., Rodriguez, J.M., Cottier, S.M., Combs, C.S., Bathel, B.F., Weisberger, J.M., Jones, S.B., Schmisseur, J.D., Kreth, P.A.: Modal Analysis of Cylinder-Induced Transitional Shock-Wave/Boundary-Layer Interaction Unsteadiness. AIAA J. 60, 2730–2748 (2022). https://doi.org/10.2514/1.J060880
- 41. Hilberg, D., Lazik, W., Fiedler, H.E.: The application of classical POD and snapshot POD in a turbulent shear layer with periodic structures. Appl. Sci. Res. 53, 283–290 (1994). https://doi.org/10.1007/BF00849105
- 42. Nakamura, Y., Sato, S., Ohnishi, N.: Application of proper orthogonal decomposition to flow fields around various geometries and reduced-order modeling. Comput. Methods Appl. Mech. Eng. 432, 117340 (2024). https://doi.org/10.1016/j.cma.2024.117340
- 43. Belson, B.A., Tu, J.H., Rowley, C.W.: Algorithm 945: modred—a parallelized model reduction library. ACM Trans. Math. Softw. 40, 30:1-30:14 (2014). https://doi.org/10.1145/2616912

- 44. Welch, P.D.: The use of fast Fourier transform for the estimation of power spectra: A method based on time averaging over short, modified periodograms. IEEE Trans. Audio Electroacoustics. 15, 70–73 (1967). https://doi.org/10.1109/TAU.1967.1161901
- 45. Hekmati, A., Ricot, D., Druault, P.: About the convergence of POD and EPOD modes computed from CFD simulation. Comput. Fluids. 50, 60–71 (2011). https://doi.org/10.1016/j.compfluid.2011.06.018
- 46. Kolesnik, E.V., Smirnovsky, A.A., Smirnov, E.M.: Compressibility effect on heat transfer intensified by horseshoe vortex structures in turbulent flow past a blunt-body and plate junction. J. Phys. Conf. Ser. 1565, 012104 (2020). https://doi.org/10.1088/1742-6596/1565/1/012104
- 47. Zhang, H., Xiao, Y., He, K., Lyu, K., Chen, Z., Zheng, C.: The 3D flow characteristics of a sonic transverse jet in laminar supersonic crossflow. Aerosp. Sci. Technol. 167, 110661 (2025). https://doi.org/10.1016/j.ast.2025.110661
- 48. Xiao, Y., Zhang, H., Chen, Z., Zhang, H., Zheng, C.: Numerical investigation on the transverse jet into a supersonic crossflow with different pressure ratios. Eng. Appl. Comput. Fluid Mech. 18, 2354760 (2024). https://doi.org/10.1080/19942060.2024.2354760
- 49. Karpuzcu, I.T., Levin, D.A., Jewell, J.S.: A Study on Side Jet Interactions for a Hypersonic Flow using Kinetic and Experimental Methods. In: AIAA SCITECH 2023 Forum. American Institute of Aeronautics and Astronautics (2023)
- 50. Dickmann, D.A., Lu, F.K.: Jet in supersonic crossflow on a flat plate. In: 25th AIAA aerodynamic measurement technology and ground testing conference. American Institute of Aeronautics and Astronautics, San Francisco, CA (2006)
- 51. Clemens, N.T., Narayanaswamy, V.: Low-Frequency Unsteadiness of Shock Wave/Turbulent Boundary Layer Interactions. Annu. Rev. Fluid Mech. 46, 469–492 (2014). https://doi.org/10.1146/annurev-fluid-010313-141346